ATOMIC FORCE MICROSCOPY—AFM

1. Principles of Atomic Force Microscopy

The atomic force microscope (AFM) was invented in 1986 at Stanford University by Binnig, Quate, and Gerber (1) as a means of measuring interatomic forces. Their invention was based on a commonly used tool called a profilometer. In this device, a stylus attached to a spring is placed in contact with any relatively flat sample to be examined. The stylus is dragged along the surface of the sample and the deflection of the spring, measured with a variety of techniques, is translated into an image of the sample surface. To create the AFM, Binnig and coworkers (1) used an extremely small cantilever as the spring, a diamond as the stylus or "tip", and a second tip to measure and control the position of the cantilever via a tunneling current. The tunneling mechanism, being exponential in tip–sample distance, made it possible to measure displacements as small as 10^{-3} nm. Since a change of 0.1 nm in the tunneling gap can change the tunneling current by one order of magnitude, a slight lateral drift of the second tip relative to the cantilever will give rise to a false reading of the position of the second tip, rendering the AFM system unstable. Because of this and other reasons, it was

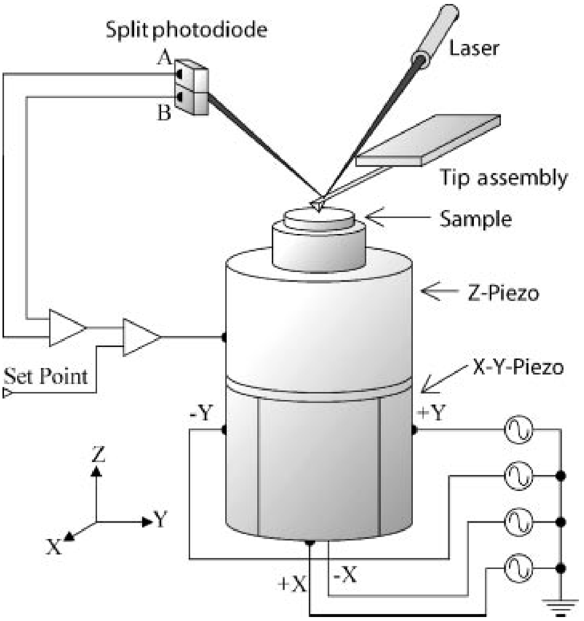

Fig. 1. A schematic diagram of a typical AFM system showing the piezoelectric tube scanner with its electric contacts, the sample mounted on top of the scanner, the tip assembly, and the optical elements.

found necessary to develop alternative methods for monitoring the deflection of the cantilever.

1.1. Contact Mode of Operation. Among the methods for monitoring the displacement of the cantilever in modern AFM systems, one finds optical deflection, optical interference, and cantilever-mounted strain gauges (2). Most current systems, however, are based on the optical deflection technique as shown in Figure 1. Here, a laser beam is reflected off the back surface of the cantilever and is incident on a split (usually four quadrants) photodiode. While the cantilever is in its relaxed position with its tip far from the sample, the photodiode is aligned such that the light falls equally on each quadrant. During operation of the AFM, the difference in the intensity of the signal produced by each quadrant measures the deflection of the cantilever. The most important advantage of this method relative to that using a tunneling current is that the deflection of the cantilever is now measured across a large area, adding stability and reproducibility. Also, one can attach an optical microscope above the cantilever and observe the position of the tip as the sample is raster scanned beneath it. This technique is extremely sensitive, and the resolution of the system is limited only by the shape of the tip, contamination of the sample, and cantilever thermal fluctuations. To produce an AFM image in what is called the contact mode, the sample and tip are brought into contact using a stepper motor until the cantilever deflects slightly. The sample is then raster scanned beneath the tip by applying appropriate triangle waves to the x- and y-contacts of the piezoelectric tube on which the sample is mounted. These plus the z-contact provide a fine control over all three directions of motion allowing accuracies of a fraction of an angstrom in the z direction while providing up to 100-μm travel in both lateral directions.

A typical method for obtaining an image of the sample topography is to map the cantilever deflection as the tip is scanned across the surface, assuming the photodiode voltage is calibrated in terms of the tip deflection for the particular cantilever in use. Though simple and fast, this "constant height" contact mode allows the tip-sample force to vary with the deflection of the cantilever according to Hooke's law, $F_{\text{cant}} = -k\,z$, where k is the spring constant of the cantilever and z is its deflection. Imaging of a soft sample may then show an incorrect representation of the topography as the force, and therefore penetration depth into the sample, changes.

A more accurate technique for imaging is called the "constant force" contact mode. In this mode, the initial deflection is set at a value chosen by the user, thus determining the force of contact. As the tip comes into contact with a feature on the surface of the sample, the deflection of the tip is measured and compared to the set-point deflection. The bias to the z contact of the piezoelectric tube is then adjusted to raise or lower the sample until the cantilever returns to the set-point deflection. This bias is displayed on the screen, calibrated in units of distance, to produce the topography image of the sample. With such feedback electronics, a constant deflection of the tip, and therefore force, is maintained during the whole scan leading to an accurate image of the topography even on soft samples. This technique also has the advantage that the system calibration is dependent on the z contact of the piezoelectric tube, which is rather constant, as opposed to properties of the cantilever, which varies from cantilever to cantilever. Note, however, that the imaging rate is limited by the speed of the feedback electronics and the spring constant of the cantilever.

1.2. Cantilever Assemblies.

Modern AFM cantilever assemblies, made from a variety of materials, can be purchased from several vendors. Most common today are microfabricated silicon or silicon-nitride cantilevers. Figure 2 is an FIB image of an *Olympus* brand AFM cantilever. On the left-hand side of the image is a portion of the spring-like cantilever that is typically 100–300 μm long with a spring constant of 0.01–100 N/m, depending on the application. On the right-hand side of Figure 2, pointing down, is the tip whose radius of curvature is typically 10–50 nm with a cone-angle of $\sim 15^{\circ}$. Such tips can often be processed to improve their sharpness, commonly down to a radius of 5–10 nm, providing a resolution of ~1–2 nm. The tips can be coated with various materials to harden them or to make them conducing or magnetic. Much work is also being invested in the development of single-wall carbon nanotube-based tips. These may provide a durable structure with a radius of curvature of 2–3 nm (3). Not shown in this figure is the tip substrate, a large area used to hold and manipulate the cantilever.

1.3. Tip-Sample Interactions.

To fully understand the operation of the AFM, it is important to consider the forces acting between the tip and the sample. However, the flexibility of the cantilever complicates a direct measurement of these forces. To simplify the analysis, assume a tip attached to a cantilever with infinite stiffness such that the tip–sample separation is controlled directly by the substrate–sample separation. Later, this restriction will be relaxed.

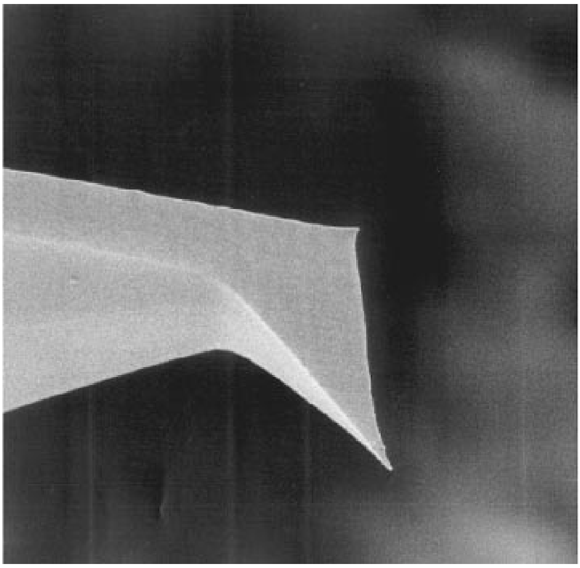

Fig. 2. An image of an *Olympus*-brand AFM cantilever with its pointed tip.

The three dominant tip–sample interactions involve the van der Waals (F_{vdW}), capillary (F_{c}), and ionic (F_{I}) forces, counteracted by the force due to the deflection of the cantilever (F_{cant}),

$$F_{\mathrm{cant}} = F_{\mathrm{vdW}} + F_{\mathrm{c}} + F_{\mathrm{I}} \tag{1}$$

Figure 3 shows a typical plot of the three forces and their sum as a function of the tip–sample separation. At large separations, these forces are negligible. At

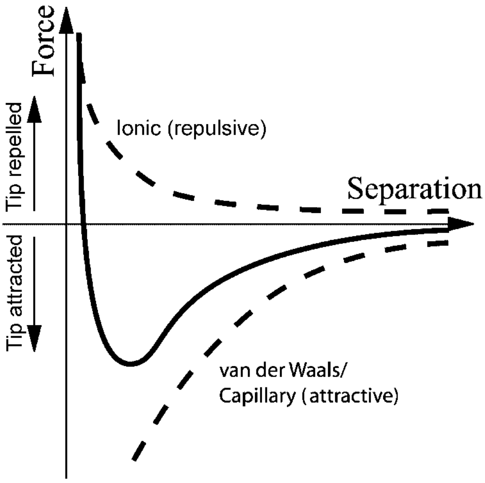

Fig. 3. Typical attractive and repulsive forces acting on the tip of a cantilever as a function of its separation from a sample under ambient conditions.

smaller separations, in vacuum or other inert environments, the van der Waals force attracts the tip toward the sample. This force is generally given in terms of the Hamaker constant, A, defined as

$$A = \frac{3}{4}kT\left(\frac{\epsilon_1 - \epsilon_2}{\epsilon_1 + \epsilon_2}\right)^2 + \frac{3I}{16\sqrt{2}}\frac{(n_1^2 - n_2^2)^2}{(n_1^2 + n_2^2)^{3/2}} \tag{2}$$

Here ϵ_1, ϵ_2, n_1, and n_2 are the dielectric constants and refractive indexes of the tip and sample and I is their ionization potential. For a sphere of radius R, separated by D from a flat surface, the force is given by

$$F_{\mathrm{vdW}} = AR/6D^2 \tag{3}$$

For example, using $A = 10^{-19}$ J, $R = 10$ nm, and $D = 0.2$ nm (tip–sample contact) yields a force of attraction of 4.1 nN.

In air, where the tip and sample are generally covered with a thin layer of physisorbed water vapor, a capillary bridge forms between the two surfaces that creates an attractive force between the tip and the sample. This force is given by (4)

$$F_{\mathrm{c}} = 4\pi R\gamma\cos\theta \tag{4}$$

Here, γ is the surface tension of the liquid and θ the angle subtended by the capillary bridge. This force is typically ~10 nN and it is commonly the case that a small concentration of a vapor forming a capillary bridge will dominate the tip–sample force.

As the tip approaches to within ~0.2 nm of the sample, or about the distance of a chemical bond, the ionic antibonding force begins to repel the tip. The ionic repulsion increases until this repulsion balances the attraction of the van der Waals and capillary forces, and the tip is said to be in contact with the sample. Further decreasing of the substrate sample separation results in an upward force on the tip. This contact force is usually kept in the range of 1–100 nN.

Although extremely useful conceptually, the type of curve shown in Figure 3 is difficult to obtain at the nanometer scale because the finite deflection of the flexible cantilever, required to measure the force, is comparable to the tip–sample separation. However, some information about the tip–sample interactions can still be obtained with a flexible cantilever by measuring the deflection of the cantilever as a function of the substrate–sample separation. Figure 4 shows such a typical curve called a force curve.

When the substrate–sample separation is large, the cantilever is not deflected. As the substrate is brought closer to the sample, attractive forces between the tip and sample increase until they are sufficient to deflect the cantilever slightly in the direction of the sample. By bending the cantilever and bringing the tip closer to the sample, the forces increase further, causing the cantilever to bend farther toward the sample. A run-away process thus snaps the tip toward the sample until the repulsive ionic force and the Hooke's law restoring

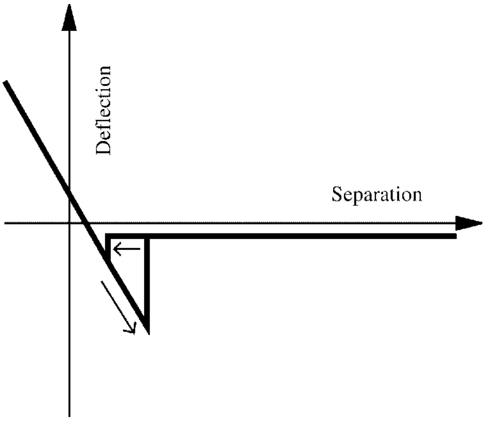

Fig. 4. The deflection of a cantilever as a function of the separation between its base and the surface of a sample. Note the hysteresis loop associated with the various forces acting on the tip.

force of the cantilever balance the attraction. At this point, the tip is in contact with the sample and further reduction of the tip–substrate separation causes a cantilever relaxation and eventually an upward deflection. On a hard sample, the cantilever will now deflect approximately as a linear function of the separation distance, and this deflection can be directly translated into a tip–sample force using Hooke's law. On a soft sample, however, the tip penetrates the sample that translates into a smaller cantilever deflection for the same change in separation distance.

As the separation is now increased, the process is reversed. However, in this case, the attractive forces act to keep the tip in contact with the sample until the cantilever's bending force overcomes the attractive forces upon which the tip snaps away from the sample. This process occurs at a greater separation than the snap-in process, thus creating a hysteresis loop.

In this manner, the measured deflection shown on the left-hand side of Figure 4 translates directly into a real measurement of tip–sample forces. Note, however, that this curve is not a measure of the tip–sample force as a function of tip–sample separation. Because the cantilever bends, the tip–sample separation is not the same as the substrate–sample separation, which the user can control. Although called a force curve, a more accurate term for Figure 4 might be a deflection curve as the interaction forces can only be measured from this curve while the tip is in contact with the sample.

1.4. Resolution.

A scanning tunneling microscope (STM), a predecessor of the AFM that requires a conducting sample, operates via a tunneling current that is exponentially dependant on the tip–sample separation distance. Therefore, the predominant contributor of current to the signal is from the very bottom of the lowest atom on the tip, with no contributions coming from atoms farther away from the sample. This tool is therefore capable of providing true atomic resolution. The tip–sample interaction of the AFM, however, is not as sensitive to distance (5,6), so atoms other then the end-most atom can contribute to the image, the number of which is dependent on the sharpness of the tip. Thus,

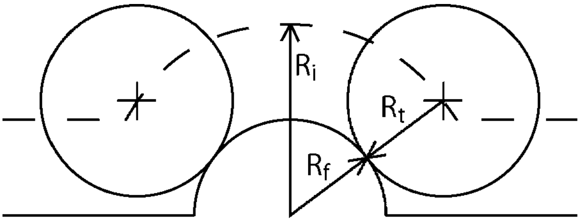

Fig. 5. An example of a tip–sample topographic convolution effect. Here, two positions of the scanning tip straddle a topographic bulge.

while many AFM images of atoms are available, most of these are due to the summation of the interactions of many atoms. The AFM, in general, cannot detect the presence or absence of individual atoms. Only under highly controlled conditions is the AFM capable of true atomic resolution (7). For large structures, in general, the resolution is mostly limited by tip–sample topographic convolution effects.

This convolution is demonstrated below in Figure 5, showing a tip of radius R_t imaging a feature of radius R_f on a sample. The resulting image of the feature has a radius of curvature of $R_i = R_t + R_f$. Thus, since we tend to think of the tip as an infinitesimal point, it appears as though this point has imaged a much larger feature.

When imaging surfaces on larger scales, say a 10–100-μm scan, with a common resolution of 512 pixels per scan line, visible features can be no smaller than ~20–200 nm. In this case, the convolution can generally be negligible. For smaller scans, a sharp tip is necessary to produce reliable images.

1.5. Noncontact Mode of Operation. The contact mode AFM operates solely within the repulsive region of the tip–sample force curve. This implies that the tip continuously applies a normal force as high as 10 μN as well as applying a shear force as a result of the tip being dragged across the surface of the sample. This mode of operation can be highly destructive to the sample, particularly in the case of soft samples such as organic or biological material.

In the noncontact mode of operation, the tip is within the attractive region of the tip–sample force curve and the interaction forces are much smaller and therefore more difficult to measure (8,9). Such an operation requires a phase-sensitive method. To that end, the tip is oscillated with an amplitude of several nanometers near its resonance frequency. This is commonly accomplished using an additional piezocrystal or a magnetic field. The force derivatives acting on the tip modify the cantilever's effective spring constant, and hence its resonance frequency and amplitude of vibration. In this manner, variations in the oscillation amplitude indicate the tip–sample separation. As with the "constant-force" mode of operation, feedback electronics is employed to adjust the sample z position until the oscillation amplitude returns to a set value. Because the tip is no longer dragged across the sample, shear forces are completely eliminated. Additionally, the normal force is limited to the much weaker attractive forces, which are on the order of 10^{-12} N. In this mode, stiffer cantilevers, such as 10 N/m, are generally desired to allow for high oscillation frequencies, typically 100–400 kHz, and to prevent the tip from snapping into the sample.

Along with variations in amplitude, it is also possible to produce images based on variations in the phase lag between the cantilever driving force and the response of the cantilever.

1.6. Intermittent-Contact Mode Atomic Force Microscopy (FM).

Although the noncontact mode of operation significantly reduces the sample damage associated with the contact mode of operation, the repulsive interaction of the latter provides a higher force and therefore higher speed. In the case of samples with large topographic features, it may be advantageous to operate in the intermittent-contact mode of operation (10–13). In this mode of operation, the tip is still vibrated. However, here the tip is repeatedly brought from the attractive region into the repulsive region of the tip–sample force curve. Therefore, while increasing the interaction force to that near the contact mode of operation, the shear forces of the contact mode of operation are still avoided. This mode is commonly called the Tapping Mode by Digital Instruments or Intermittent Mode by other companies.

1.7. Manufacturers.

Atomic force microscopy systems and components are manufactured by several companies. The largest supplier is currently the Veeco Metrology Group, which was formed by aquiring Digital Instruments and WyKo, Topometrix, Thermomicroscopes, Advanced Surface Microscopy, JPK Instruments, K-TEK International, MikroMasch, Molecular Imaging Corporation, NanoDevices, Nanosurf, NANOSENSORS, Novascan Technologies, NT-MDT, Omicron Vacuumphysik, Quesant Instruments, RHK Technology, Surface Imaging Systems, and Triple-O Microscopy.

2. Variants of Atomic Force Microscopy

The three basic modes of operation of the AFM provide different techniques for mapping the topography of a surface. However, the AFM has proven to be a useful base for a wide range of related techniques for mapping other qualities of a sample including, eg, electrical properties, thermal conductivity, elasticity, and friction.

2.1. Scanning Capacitance Microscopy.

One technique used for electrical characterization of semiconductor materials is scanning capacitance microscopy (SCM) (14). This technique maps the tip–sample capacitance at a given voltage at every point in the scan using the contact mode of operation. Such a measurement can yield the local doping level of semiconductor substrate.

In general, the capacitance in the vicinity of a conducting tip AFM is determined by applying an ac bias across the tip–sample and measuring the current flow with a lock-in amplifier. Theoretically, the total capacitance of a metal–oxide–semiconductor (MOS) system, C_{tot}, is given as the series capacitance of the oxide, C_{ox}, and the depletion region, C_{D}. A standard C–V curve is obtained by applying a slowly sweeping dc bias to adjust the depletion depth and a small ac bias to measure the capacitance. In the high frequency ac limit, where charge carriers do not have time to collect under inversion, C_{D} can be approximated in terms of the depletion depth, $C_{\mathrm{D}} = \varepsilon_{\mathrm{Si}}/x_{\mathrm{D}}$, where the depletion depth, x_{d}, is given by (15)

$$X_D = \sqrt{\frac{2\varepsilon_{\mathrm{Si}}\psi_s}{qn_p/p_p}} \tag{5}$$

Here, ψ_s is the potential drop between the silicon bulk and the silicon/oxide surface and $n_{\mathrm{p}}/p_{\mathrm{p}}$ the ratio of minority to majority carriers in the substrate. In the low frequency ac limit, where minority carriers collect in the inversion region, C_{D} is given by (15)

$$x_D = \frac{\varepsilon_{\mathrm{Si}}}{\sqrt{2}L_{\mathrm{D}}} \frac{1 - e^{-\beta\psi_s} + n_p/p_p(e^{\beta\psi_s} - 1)}{\sqrt{(e^{-\beta\psi_s} + \beta\psi_s - 1) + n_p/p_p(e^{\beta\psi_s} - \beta\psi_s - 1)}} \tag{6}$$

where L_{D} is the Debye length and $\beta = q/K\mathrm{T}$. In both cases, the surface potential, ψ_s, is given in terms of the applied dc bias. Early experiments in SCM imaging were performed at a fixed dc bias in the high frequency limit, providing a measure of C_{tot}. In modern systems, a second medium-frequency bias is added to measure dC_{tot}/dV to provide a greater signal-to-noise ratio by measuring the signal at a frequency above the most prevailing noise contributions.

2.2. Tunneling AFM. A standard technique for characterizing MOS devices on large-scale areas consists of obtaining *I–V* curves across mmeter-size metal disks fabricated on the surface of the sample. Here, the bias swings are larger than the work function of the media involved (~4 V), namely, under the Fowler-Nordheim current emission regime. These *I–V* curves provide information on charge trapping, dielectric strength, and oxide degradation. In its standard form, however, this technique lacks the required resolution. Therefore, a new form of AFM has been developed that uses a conducting tip and a constant tip–sample bias that gives rise to a varying tunneling current through a thin dielectric film. Such an AFM is called a tunneling atomic force microscope (TAFM) or TUNA by Digital Instruments. Here the tunneling current depends on the local thickness of the probed dielectric, making it possible to obtain dual maps of the topography of the top and bottom surfaces of the dielectric, as well as a map of the thickness or electrical quality of the dielectric, all at a resolution equaling approximately the thickness of the dielectric (16). The utility of the TAFM has been demonstrated by several groups who use it routinely for the characterization of the local thickness and dielectric strength of thin silicon oxide and nitride films, and carbon contamination of oxides on silicon (16–25).

Electron Tunneling. MOS devices are typically fabricated on doped silicon that is thermally oxidized to produce a few nanometers-thick oxide. To control the generation of a conducting channel in the silicon beneath the oxide, a metal or polysilicon gate is fabricated above the oxide. If a large enough bias is placed across the thin barrier layer, such as the oxide in the MOS structure, quantum mechanical tunneling of electrons occurs through the layer. This process has been studied extensively (26–33). The total tunneling current through the dielectric, *I*, is determined by integrating over all electrons with the probability of any electron tunneling through the barrier determined by the WKB approximation (34,35),

$$I = A_{\mathrm{eff}} \frac{e^2}{2\pi h \Delta d^2} \left[\bar{\phi} \exp\left(\sqrt{\frac{8m_{\mathrm{eff}}}{\hbar^2}} \Delta d \sqrt{e\bar{\phi}} \right) - (V_{\mathrm{ox}} + \bar{\phi}) \exp\left(-\sqrt{\frac{8m_{\mathrm{eff}}}{\hbar^2}} \Delta d \sqrt{e(V_{\mathrm{ox}} + \bar{\phi})} \right) \right] \tag{7}$$

Here, A_{eff} is the effective tunneling area, e the electron charge, ϕ is the average barrier height, V_{ox} is the bias across the oxide that is dependent on the flat-band

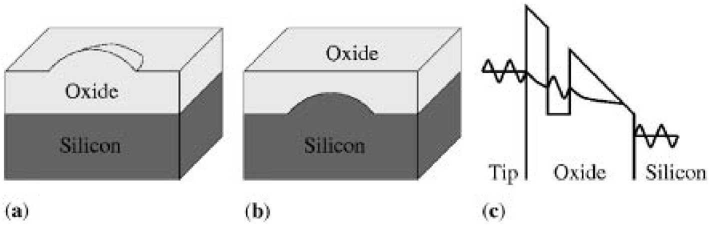

Fig. 6. A depiction of possible dielectric structures and their expression as revealed by AFM and TAFM images of the same area: Case (**a**) shows a silicon–oxide interface that is flat yet the oxide has a bulge. In case (**b**), the silicon–oxide interface has a bulge yet the oxide is flat. In case (**c**), there is a localized lowering of the dielectric conduction band, possibly due to an impurity.

voltage and thus the substrate doping, Δd is the distance through which the electron must tunnel, m_{eff} is the effective mass of the electron in the oxide, and $\hbar$ is Planck's constant. Although this equation is derived for parallel-plate metal electrodes and is being applied to a case where one electrode is a semiconductor and the other is a curved-tip surface, it is still accurate enough for a simple treatment.

Image Interpretation. The TAFM uses a conducting probe scanned over a dielectric of interest to produce images containing features that are interpreted as variations in one or more of the parameters mentioned earlier. In most cases, the dominant variation is assumed to be the change in the oxide thickness, d.

Figure 6 illustrates how features observed in TAFM images can be interpreted in terms of dielectric features. Figure 6**a** shows a case where the silicon–oxide interface is flat yet the oxide has a bulge. The thickened oxide reduces the current flow at a constant applied bias, which can be detected by both tunneling and topography maps. A defect on the surface that is buried, such as that shown in Figure 6**b**, increases the current flow at a constant applied bias and so will be observed by the tunneling system but not by the AFM. Finally, the feature in Figure 6**c** depicts a localized lowering of the conduction band, possibly due to an impurity, effectively decreasing the tunneling length and therefore the tunneling resistivity. This local effect may again not be observed as a topographic feature, as observed by the AFM. To distinguish between these three cases, one needs therefore to analyze both AFM and TAFM maps.

Current Feedback. Although a constant bias applied between tip and sample allows some imaging to be performed, it is easy to conceive of cases where this mode is not desirable. The reason is that since the tunneling equations are depend exponentially on the ratio of the applied bias and the oxide thickness, a sample containing both thin and thick regions of the oxide can cause the current to rapidly swing from below the noise level to above the range of the current detector, producing only a small range of sensitivity. On the other hand, maintaining a constant tunneling current across the oxide yields a direct, linear map of the thickness of the oxide. Note that such an interpretation breaks down at extremely thin oxides. Note, on the other hand, that forcing a current through an oxide can create charge-trapping centers that affect the tunneling current. Constant current imaging, however, makes this effect uniform over the surface

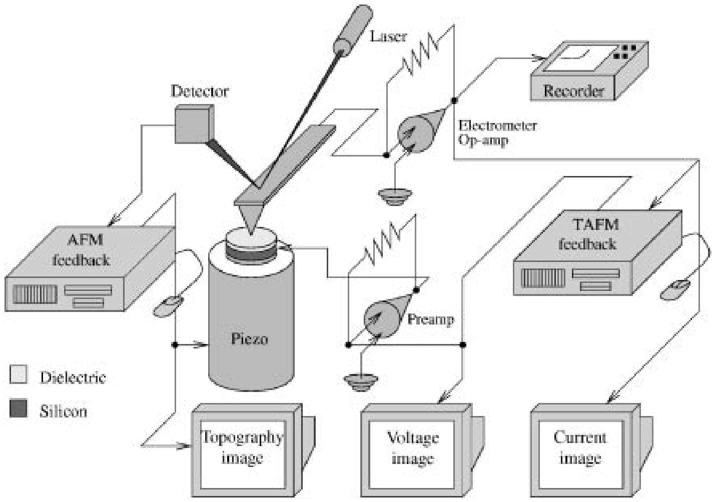

Fig. 7. A schematic diagram of the TAFM system showing the dual feedback electronics, one for the AFM and one for the TAFM.

of the sample, avoiding the large currents associated with a constant-voltage imaging of thin oxides. Care must be taken in controlling the current density during imaging while maintaining a reasonable scan speed. The TAFM system discussed here operates in a constant (fA-range) current mode where a second feedback electronics controls the applied tip−sample bias.

Experimental System. Figure 7 is a schematic diagram of the TAFM system. The system uses a conventional AFM (36) to map the surface of a dielectric with areas that can be as large as 100 × 100 μm^2. For obtaining TAFM maps, a standard silicon or silicon−nitride cantilever is replaced with a conducting cantilever and the area is scanned while applying a tip−sample bias. A second, independent, computer-controlled feedback system (37) simultaneously monitors the tip−sample tunneling current through the dielectric and adjusts the applied positive sample bias to maintain a constant 100-fA set-point current. This current is detected by a preamplifier that is capable of sensing currents as small as 10 fA with a bandwidth of 1 kHz. This amplifier can be based, eg, on the Burr Brown OPA128LM electrometer op-amp. As the tip or sample is raster scanned, the bias required to maintain a constant current is recorded and displayed as a local resistivity map of the oxide with a resolution approximating the thickness of the film. Imaging is usually performed by injecting electrons from the silicon−dielectric interface rather than the tip, providing a reasonably uniform barrier height. The effective electron mass and contact area are also assumed to be constant. Thus, features observed in TAFM images can be attributed to changes in the dielectric thickness and the doping of the substrate.

This system is also capable of producing I−V curves at a chosen location by using the AFM to position the tip at a particular location, ramping the applied bias and recording the current. The bias is ramped back to 0 V once a preset current is reached. The AFM feedback electronics maintains a constant contact tip−sample area by maintaining a constant force on the tip thus producing a

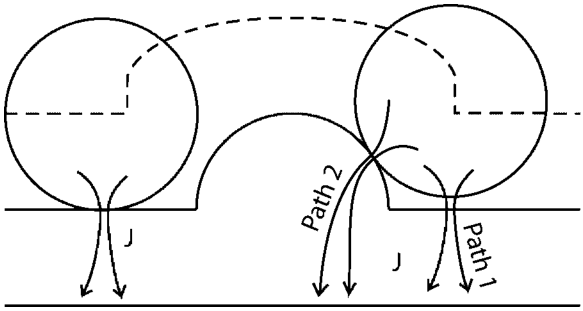

Fig. 8. An example of a TAFM tip–sample topographic and electronic convolution. Here, tunneling between the tip and sample can occur also from the sides of the tip.

conventional AFM image. The entire system is enclosed within a bell jar for environmental control and a Faraday cage for electrical noise reduction.

TAFM Tip Convolution. In the same manner as AFM imaging, TAFM imaging can suffer from tip–sample topographic convolution. However, where AFM convolution is a relatively simple addition of the radii of the probed surface feature and the tip in a given direction, the TAFM convolution is more complex, as shown in Figure 8. When the tip is in direct contact with a flat surface surrounding a feature, the current flows in a continuum of paths directly down through the dielectric as shown on the left-hand side of Figure 8. Upon contacting the feature, the tip lifts off the flat surface, as shown on the right-hand side of Figure 8. At this point, one might imagine that if the tip lifts 1.5 nm above a 5-nm thick feature, than the resulting current would indicate a 6.5-nm thick feature. There are two complications that prevent this from being the case. One is the addition of a vacuum barrier in the original path and the other is the addition of a second continuum of paths contributing to the total current. These two groups of paths are labeled in Figure 8 as Path 1 and Path 2.

The deviation of the current from values expected from a simple increase in the dielectric feature to 6.5 nm is a complex balance between the added vacuum barrier shown as Path 1 and the added path length shown as Path 2. A complete solution to this problem would require a self-consistent accounting of these two sets of paths including consideration of oxide charging. Nevertheless, it is reasonable to assume that as the tip lifts from the surface, there is a shift from Path 1 to Path 2 until Path 2 is the viable one at the top of the feature. Further analysis of this problem, however, is beyond the scope of this work.

Example. Consider an example of a TEM image of a gate oxide with a thinning defect, as shown in Figure 9 (Produced by Siemens). Conventionally, obtaining a transmission electron microscopy (TEM) image requires sectioning the sample and thereby destroying it. The tunneling map of the oxide, however, Figure 10, obtained by TAFM, depicts this defect as a peak, indicating lowered tunneling resistivity were the oxide narrows. Note that unlike the TEM, the TAFM image was produced without damaging the probed device.

Conclusion. The TAFM has been developed as a method for locating and characterizing defects in thin dielectrics. Its ability to do so has been demonstrated on both a manufacturing defect, in this case a MOS capacitor, and

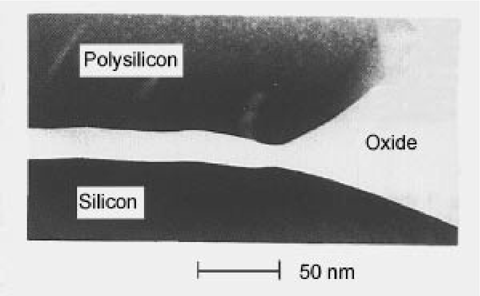

Fig. 9. A TEM image revealing an oxide defect. Note that here the sample had to be cut exactly at the defect site.

on contaminated samples. Although currently useful as a tool for qualitative analysis, continued development would help to improve quantitative analysis. In particular, the issue of sample charging needs to be addressed further as this is a significant effect on the imaging process. For example, it might be possible to determine under what conditions charging could be reduced or eliminated. Alternately, it may be possible to account for this effect rather than eliminating it. Solving the problem of charging should dramatically improve the TAFM calibration and make the tool even more useful.

2.3. Scanning Spreading Resistance Microscopy. Scanning spreading resistance microscopy (38–42) is another technique for profiling doped semiconductor structures using a conductive-tip AFM in the contact mode of operation. Here, one applies a bias across the tip–sample and the resulting current through the sample is measured with a logarithmic amplifier as the tip is scanned. The current, for a given bias, is proportional to the product of free carrier concentrations and mobility near the location of the tip. These are determined by the doping concentration, and thus a high resolution map of the surface of a semiconductor structure can be generated by moving the tip in controlled fashion across the surface, assuming all dopants are electrically active.

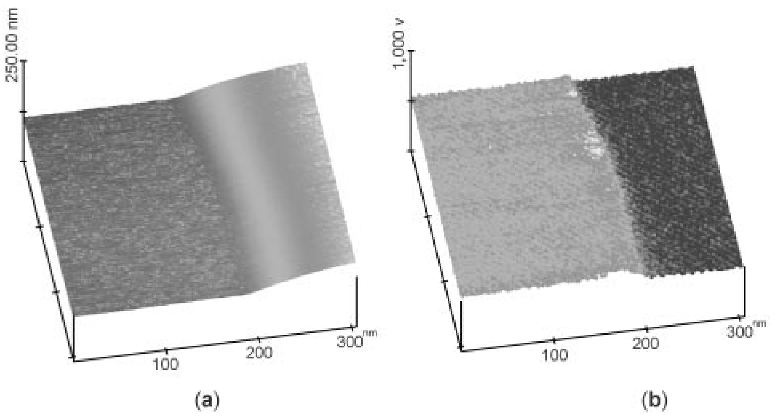

(a) (b)

Fig. 10. AFM (**a**) and TAFM (**b**) images of a defective oxide. The TAFM image reveals the defect as a change in tunneling, which is transparent to the AFM.

Typically, this method is applied to the cross-section of semiconductor device structures.

2.4. Lateral Force Microscopy. One of the problems associated with the operation of a contact-mode AFM is a twisting of the cantilever as it is pulled across the sample. The degree of twisting is a function of the tip–sample friction that in turn is a function of the tip and sample materials. Lateral force microscopy (43) scans the sample such that this twisting is along the axis of the cantilever. Using an additional set of photodetectors, namely, a quadrant structure, yields a measure of changes in friction due to the sample material.

2.5. Electric/Magnetic Force Microscopy. Electric force microscopy is based on the use of a conducting-tip AFM to map the tip–sample electric field, while the magnetic counterpart uses a tip whose apex is magnetized (44–47). With the AFM operating in the noncontact mode, these forces, which are stronger than the van der Waals force, act through their derivatives to modify the resonant frequency of the vibrating cantilever. The modification of the resonance frequency for a constant driving frequency gives rise to changes in the cantilever amplitude of vibration that is proportional to the local electric or magnetic field.

2.6. Kelvin Probe Microscopy. Kelvin probe microscopy (48–50) is a technique for measuring the relative work function of a sample and tip. To perform this measurement, an ac bias is applied between a conducting tip and sample to vibrate the cantilever. In this way, the AFM is in a noncontact or intermittent-contact mode. The force between the cantilever and the sample is given by

$$\begin{aligned} F &= 1/2dC/dz(V_{\mathrm{dc}} + V_{\mathrm{ac}}\sin\omega t)^2 \\ &= 1/2dC/dz(V_{\mathrm{dc}}^2 + 2V_{\mathrm{dc}}V_{\mathrm{ac}}\sin\omega t + 1/2V_{\mathrm{ac}}^2 - 1/2V_{\mathrm{ac}}^2\cos 2\omega t) \end{aligned} \tag{8}$$

Here, C is the tip–sample capacitance, V_{ac} is the applied tip–sample ac bias, and V_{dc} is the applied dc bias plus the work functions of the tip and sample. From this equation, one observes that the strength of the harmonic at the frequency of the applied ac bias is dependent on the strength of the dc component. Thus, by applying an additional dc bias that negates these work functions, the ac term can be canceled so that the tip oscillates at twice the frequency of the applied ac bias. This is performed by using a lock-in amplifier to measure the signal at the frequency of the applied ac bias that in turn generates the negating signal that is a measure of the relative work functions.

2.7. Force Modulation Microscopy. This AFM variant (51) is operated in a constant-force contact mode with a small oscillation that is applied to the tip at a frequency higher than the frequency response of the feedback electronics of the AFM. However, the amplitude of oscillation of the tip, which is in direct contact with the sample, is a function of the elasticity of the sample. Therefore, a topographic image is obtained from the slow feedback loop while an elasticity map of the sample is obtained from the faster oscillation amplitude using a lock-in amplifier.

2.8. Scanning Thermal Microscopy. Scanning thermal microscopy (52,53) is a method for measuring the thermal conductance of a sample that exhibits usually a lower resolution than obtained by other AFM techniques. In this AFM variant, a resistive heating element is bent into a V-shaped structure that is used as the AFM tip. A current applied to the element heats it to a temperature above that of the sample where some of this heat is dissipated by the thermal conductance of the sample. This effect can be expressed as $Q = -k(T_{\text{tip}} - T_{\text{samp}})$, where Q is the heat generated by the tip, which is proportional to the bias applied to the element. Therefore, the bias required to maintain a given temperature is indicative of the sample thermal conductivity.

3. Examples of Atomic Force Microscopy Applied to Semiconductors

Dielectric breakdown of thin gate oxides fabricated on silicon wafers is, in general, a result of a large variety of defects including, eg, particulate contamination, pinholes, and surface roughness. One particular limiting factor affecting the quality of these oxides results from the presence of a variety of metallic islands introduced during wafer processing. Low concentrations of copper in particular have been observed to cause defects when the copper was deposited from hydrofluoric acid (HF) solutions in ultrathin oxides (54–57). For example, for 3-nm oxides, $<1 \times 10^{10}$ atoms/cm^2 copper deposited on the silicon surface from contaminated HF are required prior to oxidation to adversely affect time-dependent dielectric breakdown (TDDB) measurements (58).

Copper deposition from HF occurs via an electrochemical redox reaction (59–66). The Cu^{2+} ions in HF solution, upon contact with a silicon surface, are reduced and deposited at nucleation sites on the silicon. The oxidation reaction takes the form of etching of the silicon surface and as the evolution of hydrogen, which is catalyzed by the presence of copper on the silicon surface. It is the second reaction that is the dominant cathodic reaction (66,67),

$$\begin{array}{ll} \text{Cathodic reactions :} & \begin{array}{c} \text{Cu}^{2+} + 2\text{e}^- \rightarrow \text{Cu} \\ \text{Cu} + 2\text{H}^+ + 2\text{e}^- \rightarrow \text{Cu} + \text{H}_2 \end{array} \\ \text{Anodic reaction :} & \text{Si} + 6\text{HF} \rightarrow \text{H}_2\text{SiF}_6 + 2\text{H}^+ + \text{H}_2 + 2\text{e}^- \end{array} \tag{9}$$

The reduction in oxide quality due to copper-contaminated HF solutions has been found to be due to the roughening of the silicon surface prior to oxidation (58,67). Removal of the copper itself with a hydrochloric peroxide mixture (HPM or RCA-2) clean, used to remove noble metals, fails to improve the oxide quality significantly implying that the roughening of the surface due to the dissolution of silicon is the cause of oxide failure, not the presence of copper formations.

3.1. AFM Imaging of Silicon Etching. An important question, however, is Where does this etching occur? Researchers have observed that silicon dissolution occurs primarily next to copper precipitation (60,61). Figure 11 is an AFM image of a sample contaminated with an HF solution containing high levels of copper. The image shows pits resulting from significant amounts of silicon being removed. This figure is also one of the first demonstrations of a “moat”, namely, a ring of etched silicon surrounds a region of material that is higher than

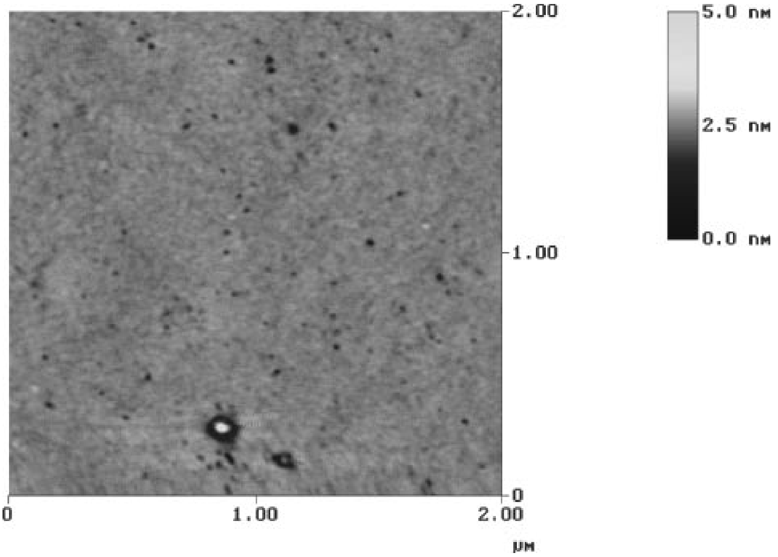

Fig. 11. An AFM image of copper-etched pits surrounded by moats.

the surrounding region. Common sense would suggest that the feature rising above the background consists of a copper deposit. However, AFM examinations of contaminated samples that have been cleaned in either HF or HCl to remove copper show that the surface features remain intact. This result indicates that silicon dissolution occurs not directly beneath the copper deposit but in the area surrounding it, while the silicon beneath the copper is protected from etching. Such a process is shown schematically in Figure 12, where the dashed line

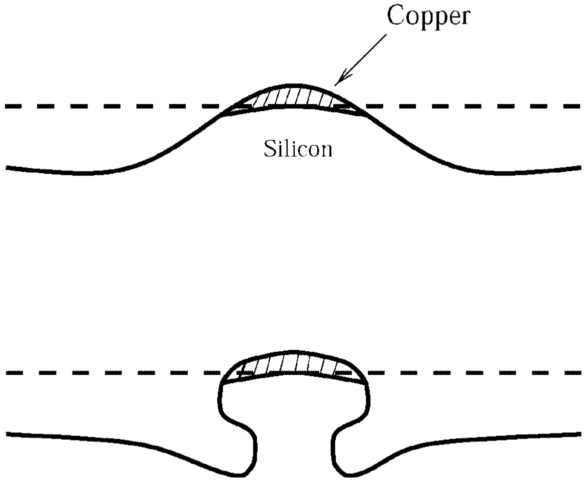

Fig. 12. Two cross-sections of features associated with the cleaning process where the dashed line represents the original silicon height. The top figure refers to a low contamination level that produces little undercutting. The bottom figure refers to a high contamination level that produces a noticeable undercutting.

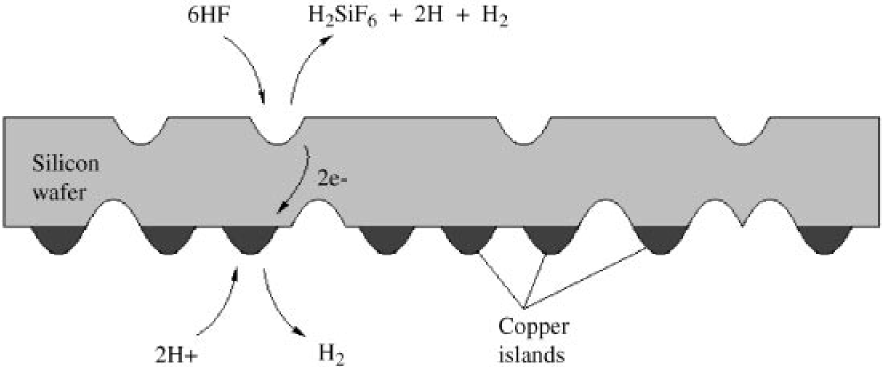

Fig. 13. A diagram of copper-catalyzed silicon etching depicting the silicon wafer, the copper islands and the electrochemsitry involved in the process.

represents the original silicon height. At lower contamination levels, little undercutting occurs and the small copper deposit causes the formation of a large silicon feature beneath it. At higher contamination levels, undercutting occurs and eventually the copper deposit is completely removed, leaving a pit in its place.

Although most silicon dissolution resulting from copper contamination is local, some dissolution also occurs at large distances from the precipitation sites. In particular, the electrochemical reactions suggest that the presence of metallic copper on the unpolished side of a wafer will catalyze hydrogen evolution on the polished side. As a result, the accompanying silicon dissolution will occur on both surfaces of the wafer, as illustrated in Figure 13. Using AFM, verified experimentally that the presence of copper on the unpolished side gave rise to roughening of the polished side, and that roughening caused oxide fails. It was also shown that the presence of hydrochloric acid (HCl) in an HF solution dissolved metallic copper on the wafer before the surface could become significantly rough (68).

Experiment. Photoresist was spun on the front sides of several silicon wafers to protect them from copper deposition. The wafers were then dipped in Cu contaminated HF depositing a small amount of copper on the unpolished sides. After rinsing, some wafers were dipped in uncontaminated HF and some in uncontaminated HF and HCl. This caused the redox reaction to occur. In particular, this includes the etching of silicon on the front side of the wafer. After another rinse, some wafers were thermally oxidized to a thickness of 3 nm for oxide defect analysis.

Results. The resulting wafers were characterized using a Digital Instruments tapping-mode AFM. Figure 14 depicts typical AFM images of (**a**) a raw wafer, w0, (**b**) contaminated wafer without HCl, w2, and (**c**) contaminated wafer with HCl, w3. A z height of 2 nm is represented by a black-to-white contrast in these images. These results show slight roughness of the surface of the reference wafer, however, there is obvious increases in roughening on the test wafer placed in uncontaminated HF. Note that although the additional roughness in Figure 14**b** appears to be due to "particles", the vertical and lateral scales must be considered. The apparent lateral scale of these features is 30–50 nm

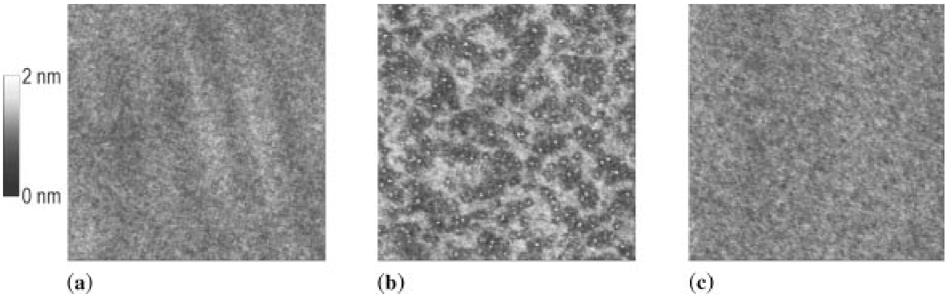

Fig. 14. Three randomly chosen AFM images covering an area of 3×3 μm. (**a**) A raw wafer, (**b**) a contaminated wafer without HCl, and (**c**) a contaminated wafer with HCl.

while the apparent vertical scale is <2 nm. Since the shape of each feature is different, tip convolution can be ruled out. It is concluded that what appears as particles is simply surface roughness. However, the HCl appears to significantly reduce this effect. It appears from Figure 14**b** that the etching process commonly produces a central island surrounded by a moat, further supporting the process suggested in Figure 12, since it is known that no copper is present on the front surface of the wafer.

Figure 15 shows a two-dimensional (2D) isotropic power spectral density (PSD) of all of the data. A technique based on a Fourier transform of the image, the PSD plots the contribution to the image as a function of wavelength and is an excellent method for quantifying surface roughness. Values of PSD on the right-hand side of the plot indicate the presence of low frequency, long wavelength features. In AFM measurements, high values here are typically an indication of drift or nonlinearities in the scanning piezoelectric tube and should not be compared between scans. Peaks on the left-hand side of the PSD plot indicate the presence of high frequency, short wavelength features. These are likely due to incompletely damped vibrations present during scanning.

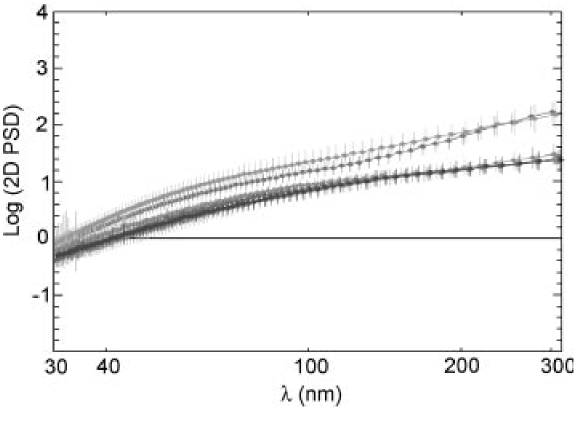

Fig. 15. The averaged power spectral densities of a group of samples. For details, see the text.

The PSD of AFM images are the most accurate between these extremes. For the 1- and 3-μm size images obtained in this experiment, this region is between ~30 and 300 nm and is shown in Figure 15. The lower grouping of curves represents data taken from the raw wafers and the wafers placed in HF where HCl was also present. The middle and top curves represent data taken from the test wafers placed in HF with no HCl and shows extensive roughening of the surface, particularly at wavelengths near 300 nm. This figure shows a 10-fold increase in PSD over a wide frequency range for the test wafers placed in clean HF over the raw wafers. However, the presence of HCl in the HF clearly counters the effect of the copper.

Time-dependent dielectric breakdown measurements of the oxidized wafers without HCl present during the clean confirm a marked decrease in time-to-breakdown on contaminated wafers, similar to earlier results where wafers were contaminated on their polished side (58). In this experiment, however, this degradation is observed as a result of surface roughening of the unpolished side. The use of HCl, again, was found to nearly eliminate this effect.

3.2. TAFM Characterization of Copper Contaminated Gate Oxides.

The TAFM system was used to electrically examine several samples of silicon contaminated with large quantities of copper. Of particular interest, was the direct effect of the large copper deposits on the electrical uniformity of the oxide as compared to the global weakening of the oxide due to silicon dissolution that was examined in the previous experiment. In this experiment, copper-contaminated wafers were thermally oxidized to 4–20 nm in thickness. Figure 16 depicts AFM and TAFM images of the oxide that were obtained simultaneously. Note that the AFM image quality is poor at this stage in the development of the TAFM tool. Due to the high density of defects, it is difficult to interpret the TAFM image; however, some points are worth noting. First, the highly prevalent small black dots indicate regions of high conductivity. It is likely that these result from the increased surface roughness. Second, it also appears that there are regions of lower conductivity indicated by the small white dots. These are larger copper contaminants similar to those observed in the previous sample that are slightly visible in AFM image as well.

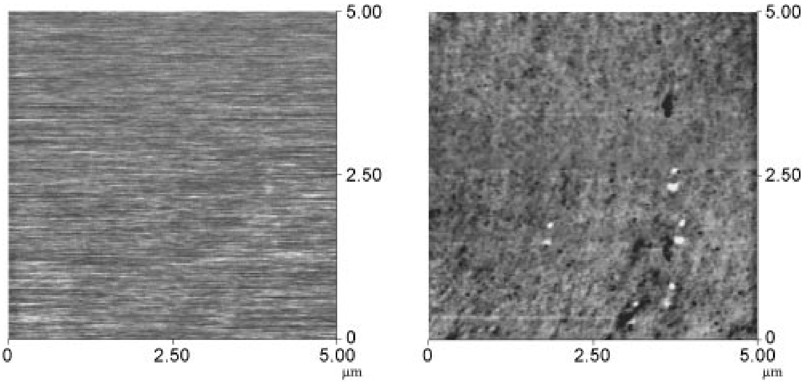

Fig. 16. AFM and TAFM images of a copper-contaminated oxide obtained simultaneously from the same area.

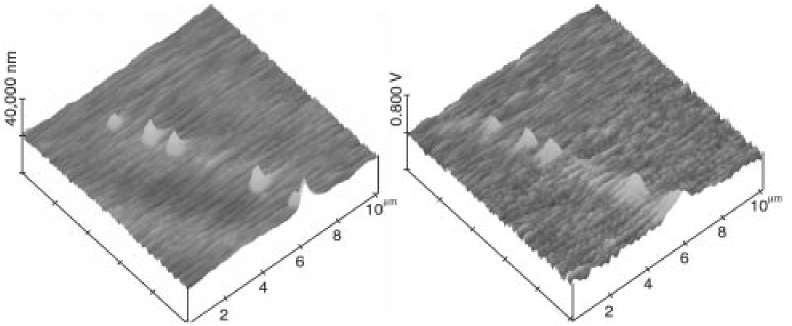

Fig. 17. AFM and TAFM images of a contaminated oxide obtained simultaneously from the same area.

Figure 17 shows another pair of simultaneous AFM and TAFM images. Here again it was found that the islands required a higher bias before the onset of tunneling and therefore would not contribute to oxide breakdown. The AFM images of the oxidized samples showed that the islands protruded ~4 nm above the surface of the already 4-nm thick oxide. The bias required to tunnel through these islands suggests that the oxide thickness was ~6 nm on top of the islands.

4. Summary

This article covered three topics: The principles of AFM, variants of AFM, and examples of AFM applied to semiconductors. The first topic discussed the three main modes of operation of AFM, namely, the contact, noncontact, and intermittent-contact (tapping) modes. Also discussed were cantilever assemblies, tip−sample interactions, and resolution and manufacturers of AFMs. Here, only the most basic concepts were addressed, concepts that will familiarize the reader with the basic phenomena involved in the very rich field of AFM. New insights and interpretations accompanied by a large body of experimental evidence have been published on the operation of the AFM since its inception in 1984, as evidenced by the publication of a large number of articles and books.

The second topic described scanning spreading resistance microscopy, lateral force microscopy, electric and magnetic force microscopy, kelvin probe microscopy, force modulation microscopy, and scanning thermal microscopy. Again, these are the most prevalent variants of AFM that can be found in every well-equipped laboratory. All of these variant are by now commercial products that can be purchased as systems operating either in ambient or under ultrahigh vacuum conditions. Also, some of these products are tailored to applied research applications and others to industrial applications that usually require more automation and the ability to handle larger samples.

The third topic deals with examples of AFM applied to semiconductors. Here, this particular choice was made because of two reasons. The first reason is that the list of examples of results obtained with AFM, even if one were to collect only the most obvious ones, is remarkably rich and could not be fit into this article. The second reason for presenting this particular choice is that the utilization of variants of AFM in new fields of technology appears at an ever growing pace. It was felt, therefore, that it will serve an important purpose to highlight one of the novel applications of AFM, the market-driving industry of semiconductors. Indeed, the shrinking of devices fabricated on a silicon chip to nanometer-scale size requires quantum mechanic considerations for the description of their operation. To characterize and check such minute structures, one has to resort to either electron microscopy or AFM. We therefore decided that it will be important to give examples of applications of AFM to the semiconductors industry.

It is hoped that this article will be found useful in presenting a tutorial of the basic principles of AFM and at the same time will wet the appetite of the reader by describing a state-of-the-art, fast-progressing application that undoubtedly will be superceded by newer applications in the near future.

BIBLIOGRAPHY

1. G. Binnig, C. F. Quate, and C. Gerber, *Phys. Rev. Lett.* **56**, 930 (1986).
2. D. Sarid, *Exploring Scanning Probe Microscopy using Mathematica*, John Wiley & Sons, Inc., Interscience, 1997.
3. H. Dai, J. H. Hafner, A. G. Rinzler, D. T. Colbert, and R. E. Smalley, *Nature (London)* **384**, 147 (1996).
4. U. Hartman, "Theory of Non-contact Force Microscopy", *Scanning Tunneling Microscopy III*, Springer-Verlag, p. 293, 1993.
5. D. J. Kellerr and F. S. Franke, *Surf. Sci.* **294**, 409 (1993).
6. J. Vesenka, R. Miller, and E. Henderson, *Rev. Sci. Instrum.*, **65**, 1 (1994).
7. F. J. Giessibl, *Science* **267**, 6871 (1995).
8. H. Ueyama, M. Ohta, Y. Sugawara, and S. Morita, *Jpn. J. Appl. Phys., Part 2* **34**, L1086 (1995).
9. S. Kitamura and M. Iwatsuki, *Jpn. J. Appl. Phys., Part 2* **34**, L145 (1995).
10. H. G. Hansma and J. H. Hoh, *Ann. Rev. Biophy. Biomol. Structure* (1994).
11. H. G. Hansma and co-workers, **15**, 296 (1993).
12. P. K. Hansma and co-workers,, *Appl. Phys. Lett.*, **64**, 1738 (1994).
13. C. A. J. Putman and co-workers, *Appl. Phy. Lett.*, **64**, 2454, (1994).
14. C. C. Williams, W. P. Hough, and S. A. Rishton, *Appl. Phys. Lett.* **55**, 203 (1989).
15. S. M. Sze, *Physics of Semiconductor Devices*, John Wiley & Sons, Inc., New York, 1981.
16. T. G. Ruskell, R. K. Workman, D. Chen, D. Sarid, S. Dahl, and S. Gilbert, *Appl. Phys. Lett.* **68**, 93 (1996).
17. M. P. Murrell, M. E. Welland, S. J. O'Shea, T. M. H. Wong, J. R. Barnes, and A. W. McKinnon, *Appl. Phys. Lett.* **62**, 786 (1993).
18. S. J. O'Shea, R. M. Atta, and M. E. Welland, *Rev. Sci. Instrum.* **66**, 2503 (1995).
19. B. Ebersberger, C. Boit, H. Benzinger, and E. Gunther, "Thickness Mapping of Thin Dieletrics with Emission Microscopy and Conductive Atomic Force Microscopy for Assessment of Dielectrics Reliability," 1996 International Reliability Symposium April 29–May 2, Dallas, Tex.
20. B. Ebersberger, C. Boit, H. Benzinger, and E. Guenther, *34th Annual IEEE International Reliability Physics Proceedings*, 1996 p. 126.
21. S. J. O'Shea, R. M. Atta, M. P. Murrell, and M. E. Welland, *J. Vac. Sci. Technol. B* **13**, 1945 (1995).

22. M. E. Welland and M. P. Murrell, *Scanning* **15**, 251 (1993).
23. F. J. Feigl, D. R. Young, D. J. DiMaria, S. Lai, and J. Calise, *J. App. Phys.* **52**, 9 (1981).
24. E. H. Nicollian, C. N. Berglund, P. F. Schmidt, and J. M. Andrews, *J. App. Phys.* **42**, 13 (1971).
25. A. Olbrich, B. Ebersberger, and C. Boit, "Nanoscale Electrical Characterization of Thin Oxides with Conducting Atomic Force Microscopy", *36th Annual IEEE International Reliability Physics Symposium*, 1998.
26. K. L. Jensen, *J. Vac. Sci. Technol. B* **13**, 516 (1995).
27. R. Waters and B. Van Zeghbroeck, *App. Phys. Lett.* **75**, 2410 (1999).
28. H. M. Gupta and M. B. Morais, *J. Appl. Phys.* **68**, 176 (1990).
29. Q. Huang, *J. Appl. Phys.* **78**, 6770 (1995).
30. Z. A. Weinberg, *Sol. Stat. Electron.* **20**, 11 (1977).
31. Z. A. Weinberg, *J. Appl. Phys.* **53**, 5052 (1982).
32. G. Krieger and R. M. Swanson, *J. Appl. Phys.* **52**, 5710 (1981).
33. M. Lenzlinger and E. H. Snow, *J. Appl. Phys.* **40**, 278 (1969).
34. D. Bohm, *Quantum Theory*, Prentice Hall Inc., New York, 1951.
35. J. G. Simmons, *J. Appl. Phys.* **34**, 1793 (1963).
36. Nanoscope III AFM system, Digital Instruments, Inc., 520 E. Montecito St., Santa Barbara, Calif. 93103.
37. Controlled with software and hardware from Intelligent Instrumentation, 6550 S. Bay Colony Drive, MS130, Tucson, Ahiz. 85706.
38. Eur. Pat. 90,201,853, (July 9, 1990), U.S. Pat. 5,585,734, (Dec. 17, 1996), M. Meuris, W. Vandervorst, and P. de Wolf.
39. P. De Wolf, T. Clarysse, and W. Vandervorst, *J. Vac. Sci. Technol. B.* **16**, 320 (1998).
40. T. Clarysse and W. Vandervorst, *J. Vac. Sci. Technol B.* **16**, 260 (1998).
41. C. Shafai, D. Thomson, M. Simard-Normandin, G. Mattiussi, and P. J. Scanlon, *Appl. Phys. Lett.* **64**, 342 (1994).
42. P. De Wolf, M. Geva, T. Hantschel, W. Vandervorst, and R. B. Bylsma, *Appl. Phys. Lett.* **73**, 2155 (1998).
43. C. D. Frisbie, L. F. Rozsnyai, A. Noy, M. S. Wrighton, and C. M. Lieber, *Science* **265**, 2071 (1998).
44. P. Grutter, *MSA Bull.* **24**, 416 (1994).
45. C. Schonenberger, S. F. Alvarado, S. E. Lambert, and I. L. Sanders, *J. Appl. Phys.* **67**, 12 (1990).
46. T. Ohkubo, J. Kishigami, K. Yanagisawa, and R. Kaneko, *IEEE Trans. J. Mag. Jpn.* **8**, 245 (1993).
47. R. Proksch, *Magnetic Force Microscopy*, Ph.D. Thesis, University of Minnesota Department of Physics, 1993.
48. H. Jacobs, H. Knapp, and A. Stemmer, *Rev. Sci. Instrum.* **70**, 1756 (1999).
49. H. Jacobs, P. Leuchtmann, O. Homan, and A. Stemmer, *J. Appl. Phys.* **84**, 1168 (1998).
50. P. Schmutz and G. Frankel, *J. Electrochem. Soc.* **145**, 2285 (1998).
51. P. Maivald, H. J. Butt, S. A. C. Gould, C. B. Prater, B. Drake, J. A. Gurley, V. B. Elings, and P. K. Hansma, *Nanotech.* **2**, 103 (1991).
52. M. Maywald, R. J. Pylkki, and L. J. Balk, *Scanning Microsc.* **8**, 181 (1994).
53. A. Hammiche, M. Reading, H. M. Pollock, M. Song, and D. J. Hourston, "Localised thermal analysis using a miniaturized resistive probe," *Rev. Sci. Instrum.* **67**, 4268 (1996).
54. S. Verhaverbeke, M. Meuris, P. W. Mertens, M. M. Heyns, A. Philopossian, D. Gräf, and A. Schnegg, *IEEE IEDM Tech. Dig.*, **71** (1991).
55. D. Ballutaud, P. De Mierry, and M. Aucouturier, *Appl. Surf. Sci.* **47**, 1 (1991).

56. W. R. Aderhold, N. Shah, S. Bogen, A. Bauer, and E. P. Burte, *Mater. Res. Soc. Symp. Proc.* **429**, 275 (1996).
57. Bert Vermeire, Lichyn Lee, and Harold G. Parks, *IEEE Trans. Semiconduct. Manufact.* **11**, 232 (1998).
58. B. Vermeire, C. A. Peterson, H. G. Parks, and D. Sarid, *Proc. Electrochem. Soc.* **99**, 69 (2000).
59. Harold G. Parks, Ronald D. Schrimpf, Bob Craigin, Ronald Jones, and Paul Resnick, *IEEE Trans. Semi. Manufacturing* **7**, 249 (1994).
60. Hitashi Morinaga, Makoto Suyama, and Tadahiro Ohmi, *J. Electrochem. Soc.* **141**, 2834 (1994).
61. L. Torcheux, A. Mayeux, and M. Chemla, *J. Electrochem. Soc.* **142**, 2037 (1995).
62. I. Teerlinck, P. W. Mertens, H. F. Schmidt, M. Meuris, and M. M. Heyns, *J. Electrochem. Soc.* **143**, 3323 (1996).
63. Oliver M.R. Chyan, Jin-Jian Chen, Hsu Y. Chien, Jennifer Sees, and Lindsey Hall, *J. Electrochem. Soc.* **143**, 1 92 (1996).
64. V. Bertagna, F. Rouelle, G. Revel, and M. Chemla, *J. Electrochem. Soc.* **144**, 4175 (1997).
65. F. W. Kern, Jr., M. Itano, I. Kawanabe, M. Miyashita, R. Rosenburg, and T. Ohmi, "Metallic contamination of semiconductor devices from processing chemicals the recognized potential," presented at the 37th Annual IES Meeting, San Diego, Calif. May 6–10, 1991.
66. G. Li, E. A. Kneer, B. Vermeire, H. G. Parks, S. Raghavan, and J. S. Jeon, *J. Electrochem. Soc.* **145**, 241 (1998).
67. S. Kunz, S. Marthon, and F. Tardif, *Proc. Electrochem. Soc.* **97**, 120 (1997).
68. I. Teerlinck, P. W. Mertens, R. Vos, M. Meuris, and M. M. Heyns, *Proc. Electrochem. Soc.* **96**, 250 (1996).

CHARLES ANTHONY PETERSON
Intel Corporation
DROR SARID
Optical Sciences Center, University of Arizona